



Article

Modeling of a Dual Air-Gap Liquid-Cooled Eddy Current Retarder Considering Transient Permeability

Wenguang Guo ^{1,*}, Bin Yan ¹ and Desheng Li ²

¹ School of Mechanical Engineering, Anyang Institute of Technology, Anyang 455000, China; 20200041@ayit.edu.cn

² College of Mechanical Engineering and Applied Electronic Technology, Beijing University of Technology, Beijing 100124, China; dsli@bjut.edu.cn

* Correspondence: 20200070@ayit.edu.cn

Abstract: This paper proposes a model for the electromagnetic performance of the dual air-gap liquid-cooled eddy current retarder (DAL-ECR) considering the transient permeability. First, the structure and working principle of the DAL-ECR are introduced. Next, the analysis model of the static air-gap flux density considering the flux leakage and end effect is established based on the piecewise function method and the magnetic equivalent circuit (MEC). Then, based on the skin effect of the electromagnetic field in the retarder, an iterative method for solving the transient permeability of the stator is proposed. According to Faraday's and Ampere's laws, the analysis model of the static air-gap flux density, and the transient permeability, the analysis model of the transient air-gap flux density is established. The braking torque of the DAL-ECR is then calculated while taking the actual path of the eddy current and the skin effect on the permeability of the stator into consideration. Finally, the calculation accuracy of the model was verified by the finite element method (FEM) and the bench test.

Keywords: air-gap flux density; eddy current braking; transient permeability; liquid cooled



Citation: Guo, W.; Yan, B.; Li, D. Modeling of a Dual Air-Gap Liquid-Cooled Eddy Current Retarder Considering Transient Permeability. *World Electr. Veh. J.* **2023**, *14*, 182. <https://doi.org/10.3390/wevj14070182>

Academic Editors: Youguang Guo, Gang Lei and Xin Ba

Received: 10 June 2023

Revised: 7 July 2023

Accepted: 11 July 2023

Published: 12 July 2023



Copyright: © 2023 by the authors. Licensee MDPI, Basel, Switzerland. This article is an open access article distributed under the terms and conditions of the Creative Commons Attribution (CC BY) license (<https://creativecommons.org/licenses/by/4.0/>).

1. Introduction

With the development of automobile technology, anti-lock braking systems (ABSs) and electronic braking systems (EBSs) have been widely used in various vehicles, which greatly improves the reliability of braking systems. However, these technologies still cannot solve the problems of high-temperature failure of the main brakes and the excessive wear of brake pads. To solve the problem of main brake failure due to high temperature and brake pad wear when heavy vehicles brake continuously on long downhills, many countries have formulated standards to apply a combined braking system on heavy vehicles, which is dominated by friction braking and supplemented by non-contact brake retarders with continuous working ability [1].

According to different working principles, retarders are mainly divided into engine braking retarders, exhaust braking retarders, hydraulic retarders (HRs), and eddy current retarders (ECRs). Compared with other retarders, ECRs have a simple structure, easy control, and fast response speed [2–4]. However, the existing ECRs have a serious heat fading of braking torque during continuous braking due to their air-cooled heat dissipation structures. To solve the above problems, some scholars propose liquid-cooled ECRs [5–7]. In these liquid-cooled ECRs with different structures, the dual air-gap liquid-cooled eddy current retarder (DAL-ECR) is a good application prospect in industrialization because of its light rotor and high braking power density [7].

The main methods to predict the braking performance of ECRs are the finite element method (FEM), the analytical method, and the magnetic equivalent circuit method (MEC). The FEM is considered to be an effective method for predicting the braking performance of the ECR [8–11], but it is expensive and time-consuming. Therefore, many scholars

choose to use Poisson's and Laplace's equations to establish the analytical models of the ECRs and to determine the coefficients of the models through the boundary conditions. The MEC is considered as a semianalytical method, which is the idea that the magnetic field is equivalent to the magnetic circuit. Compared with the FEM, the analytical method and the MEC is faster in calculation, but the calculation error is larger. Therefore, the analytical method and the MEC are often used to guidance for the preliminary design of ECRs.

Shin et al. [12], Lubin et al. [13], and Gulec et al. [14] proposed analytical models which considered the actual closed path of eddy currents, respectively, but the models ignored the end effect of the magnetic field and the heat effect on conductivity. Therefore, Jin et al. [15] and Lubin et al. [16] proposed 3D analytical models for the end effect of the ECRs, respectively. Jin et al. [17] and Ye et al. [18] proposed analytical magnetic–thermal coupling models, respectively, and their computing results agreed well with the measured results. However, the analytical methods neglected saturation of the core, and they are not suitable for the prediction of the performance of the saturation excitation ECRs for heavy vehicles. Hence, the MEC was used for the design of the ECRs by considering the magnetic saturation and electromagnetic characteristics of all materials [19–22]. Based on the MEC and the thermal resistance network method, Gulec et al. [23] proposed a magnetic–thermal coupling model considering the influence of heat on the electromagnetic properties of materials. Kou et al. [24,25] studied the electromagnetic performance of ECRs by combining the MEC with the analytical method. Despite the continuous improvement of the ECRs' calculation models, the problem of the unsteady transient permeability of the eddy current disc at different speeds was rarely considered. The change of the transient permeability is caused by the skin effect of the eddy current disc when the ECR works. The transient permeability will decrease with the increase of the ECR speed under constant excitation current, which is the key factor restricting the increase of the ECR torque at high speed. Although Guo et al. [26] considered this situation, a permeability distribution model proposed in the paper was obtained by experiments. Hence, the model inevitably increased the cost and time consumption.

Based on the introduction of the structure and working principle of the DAL-ECR, this paper presents a torque model of eddy current braking, which considers the problems of magnetic flux leakage, end effect, and the transient permeability. Based on the skin effect of the eddy current magnetic field, an iterative method is proposed to solve the transient permeability of the stator. The advantages of the transient air-gap flux density model considering transient permeability are verified by FEM. Finally, the eddy current braking torque model was verified by the bench test.

2. Structure and Working Principles

The DAL-ECR is composed of a stator with a cooling channel, a rotor with toothed salient poles, and a group of excitation coils, as shown in Figure 1. When the excitation coils are excited with direct current (DC), a magnetic flux generated by the coils passes through the upper part of the stator, the upper air gap, the rotor, the lower air gap, and the lower part of the stator to form a loop. The stator cuts the magnetic flux lines from the rotor, inducing the eddy currents. The magnetic field produced by the eddy current interacts with the magnetic field produced by the excitation coils to produce the braking torque. The heat generated on the stator during braking is taken away by coolant in the cooling channel of the stator.

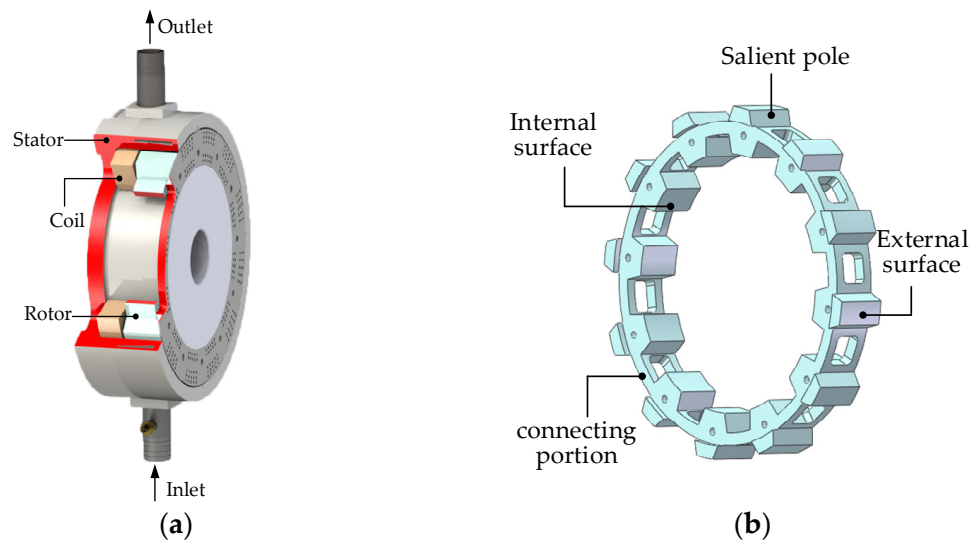


Figure 1. (a) Sectional view of the DAL-ECR. (b) Rotor of the DAL-ECR.

3. Analysis Method

To simply and intuitively show the basic ideas of the calculation model proposed in this paper, this section uses block diagrams to represent each link required for the establishment of the calculation model and uses arrows to indicate the transfer directions of each action, as shown in Figure 2. The transient permeability given in Figure 2 refers to the stator permeability of the retarder operating at different speeds and different excitation currents. The transient permeability is introduced into the model to consider the influence of the skin effect on the stator permeability.

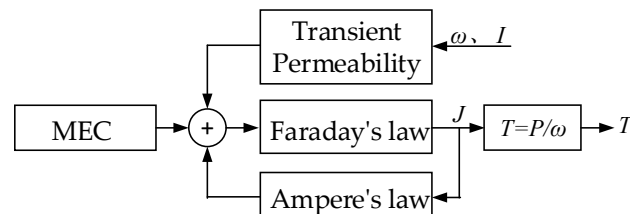


Figure 2. Schematic block diagram of the basic idea.

The model proposed in this paper is based on the model proposed in the literature [22], which takes into account the change of transient permeability with the change of current and speed. Firstly, the static air-gap magnetic density distribution is obtained by MEC considering the magnetic field end effect (in Section 3.1). Secondly, the eddy current density and the transient air-gap flux density distribution are obtained by Faraday's law and Ampere's law (in Section 3.2). Then, the transient permeability is obtained by an iterative method (in Section 3.4). Finally, the eddy current braking torque is obtained by the relationship between torque, braking power and rotational speed (in Section 3.5).

3.1. MEC Analysis Model

Due to the symmetry of the brake system, the analysis model is 1/12 of the whole actual DAL-ECR, as shown in Figure 3. The main magnetic flux and leakage flux formed by the excitation coil are shown in Figure 4. To obtain the air-gap magnetic density of the DAL-ECR, the MEC diagram is established according to the analysis model, as shown in Figure 5.

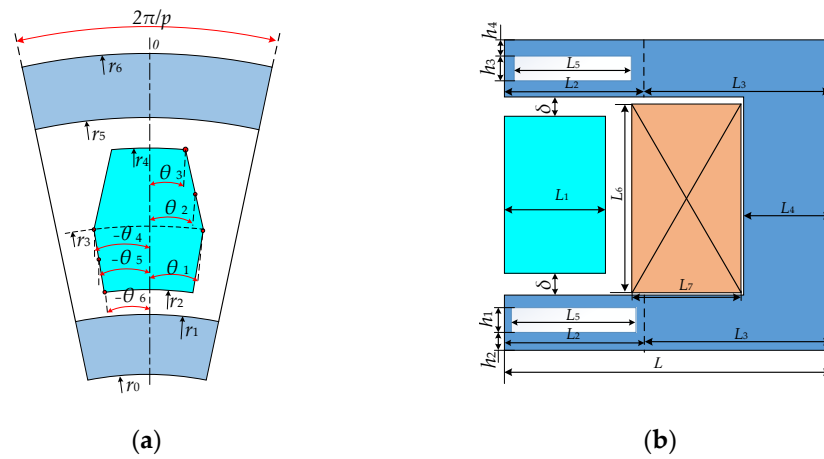


Figure 3. Analysis model of the DAL-ECR in (a) front and (b) side view direction.

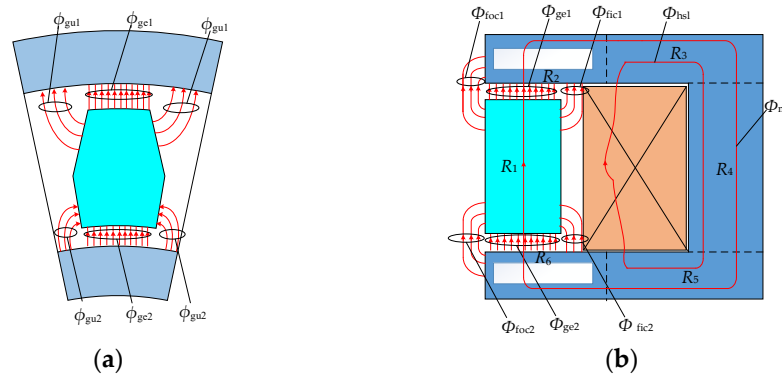


Figure 4. Main flux and leakage flux formed by the excitation coil in (a) front and (b) side view direction.

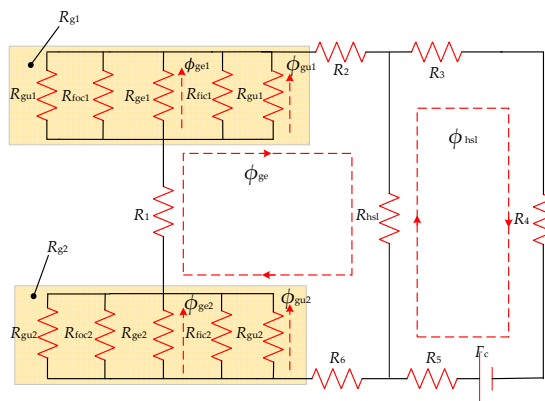


Figure 5. MEC analysis at static state.

The magnetic motive force (MMF) from the excitation coil can be obtained by

$$F_c = NI \tag{1}$$

where N is the turn number of the coil and I is the current in the coil.

According to Figures 3–5, each part of the magnetic reluctance of the DAL-ECR can be obtained by the following formulas:

$$R_1 = \frac{r_4 - r_2}{\mu_0 \mu_1 (\theta_6 r_2 + \theta_3 r_4) L_1} \tag{2}$$

$$R_2 = \frac{(L_2 - L_1/2)p}{2\pi\mu_0\mu_2[r_6^2 + h_3(h_3 + 2h_4 - 2r_6) - r_5^2]} \quad (3)$$

$$R_3 = \frac{p(L_3 - L_4/2)}{2\pi\mu_0\mu_3(r_6^2 - r_5^2)} \quad (4)$$

$$R_4 = \frac{p}{2\pi\mu_0\mu_4L_4(r_5 + r_1)} \quad (5)$$

$$R_5 = \frac{p(L_3 - L_4/2)}{2\pi\mu_0\mu_5(r_1^2 - r_0^2)} \quad (6)$$

$$R_6 = \frac{(L_2 - L_1/2)p}{2p\mu_0\mu_6[r_1^2 - h_1(h_1 + 2h_2 + 2r_0) - r_0^2]} \quad (7)$$

$$R_{g1} = \frac{R_{gu1}^2 R_{foc1} R_{ge1} R_{fic1}}{2R_{gu1} + R_{foc1} + R_{ge1} + R_{fic1}} \quad (8)$$

$$R_{g2} = \frac{R_{gu2}^2 R_{foc2} R_{ge2} R_{fic2}}{2R_{gu2} + R_{foc2} + R_{ge2} + R_{fic2}} \quad (9)$$

where p is the number of teeth of the rotor; μ_0 is the air permeability; $\mu_1, \mu_2, \mu_3, \mu_4, \mu_5$, and μ_6 are the relative permeability of R_1, R_2, R_3, R_4, R_5 , and R_6 shown in Figure 3. The permeability of each part of the DAL-ECR in the static state can be obtained by an iterative method [1,15].

The air-gap magnetic reluctance of each part in the period can be obtained by

$$R_{foc1} = \frac{1}{\int_0^w \frac{2\mu_0 r_4 \theta_3}{\delta + \pi r} dr}, w = \min(r_6 - r_5, r_4 - r_3) \quad (10)$$

$$R_{foc2} = \frac{1}{\int_0^w \frac{2\mu_0 r_2 \theta_6}{\delta + \pi r} dr}, w = \min(r_1 - r_0, r_3 - r_2) \quad (11)$$

$$R_{ge1} = \frac{2\mu_0 r_4 \theta_3 L_1}{\delta} \quad (12)$$

$$R_{ge2} = \frac{2\mu_0 r_2 \theta_6 L_1}{\delta} \quad (13)$$

$$R_{foc1} = \frac{1}{\int_0^w \frac{2\mu_0 r_4 \theta_3}{\delta + \pi r/2} dr}, w = \min(r_6 - r_5, \frac{L - L_1 - L_4}{2}) \quad (14)$$

$$R_{foc2} = \frac{1}{\int_0^w \frac{2\mu_0 r_2 \theta_6}{\delta + \pi r/2} dr}, w = \min(r_3 - r_2, \frac{L - L_1 - L_4}{2}) \quad (15)$$

$$R_{gu1} = \frac{1}{\int_0^w \frac{\mu_0 L_1}{\delta + \pi r/2} dr}, w = \min[r_4 - r_3, r_5(\pi/p - \theta_3)] \quad (16)$$

$$R_{gu2} = \frac{1}{\int_0^w \frac{\mu_0 L_1}{\delta + \pi r/2} dr}, w = \min[r_3 - r_2, r_1(\pi/p - \theta_6)] \quad (17)$$

The slot leakage flux ϕ_{hsl} is the main part of the leakage flux, as shown in Figure 4. The magnetic reluctance of the slot leakage flux can be obtained by

$$R_{hsl} = \frac{1}{\frac{4\pi\mu_0 r_3 [3(L - L_4 - L_1) - 2L_7]}{3p(r_5 - r_1)}} \quad (18)$$

According to Kirchhoff's voltage law, the following formulas can be given:

$$\phi_{ge}(R_1 + R_2 + R_6 + R_{g1} + R_{g2} + R_{hsl}) - \phi_{hsl}R_{hsl} = 0 \tag{19}$$

$$\phi_{hsl}(R_3 + R_4 + R_5 + R_{hsl}) - \phi_{ge}R_{hsl} = F_c \tag{20}$$

The static air-gap flux can be expressed as

$$\phi_{ge} = \frac{F_c}{(R_1 + R_2 + R_6 + R_{g1} + R_{g2} + R_{hsl})(R_3 + R_4 + R_5 + R_{hsl})/R_{hsl} - R_{hsl}} \tag{21}$$

$$\phi_{ge1} = \frac{R_{g1}\phi_{ge}}{R_{ge1}} \tag{22}$$

$$\phi_{gu1} = \frac{\phi_{ge}R_{g1}}{R_{gu1}} \tag{23}$$

$$\phi_{ge2} = \frac{R_{g2}\phi_{ge}}{R_{ge2}} \tag{24}$$

$$\phi_{gu2} = \frac{R_{g2}\phi_{ge}}{R_{gu2}} \tag{25}$$

Under static state, the amplitude of the air-gap flux density of each part can be expressed as

$$B_{ge1} = \frac{\phi_{ge1}}{2r_4\theta_3L_1} \tag{26}$$

$$B_{ge2} = \frac{\phi_{ge2}}{2r_2\theta_6L_1} \tag{27}$$

$$B_{gu1} = \frac{\phi_{gu1}}{2r_5(\pi/p - \theta_3)L_1} \tag{28}$$

$$B_{gu2} = \frac{\phi_{gu2}}{2r_1(\pi/p - \theta_6)L_1} \tag{29}$$

Based on the piecewise function, the upper and lower static air-gap magnetic flux densities in one period can be expressed as

$$B_1(\theta) = \begin{cases} B_{gu1} & -\pi/p \leq \theta \leq -\theta_1 \\ B_{gu1} + \alpha_1(\theta + \theta_1)^2 & -\theta_1 < \theta \leq -\theta_2 \\ B_{ge1} - \alpha_2(\theta + \theta_3)^2 & -\theta_2 < \theta \leq -\theta_3 \\ B_{ge1} & -\theta_3 < \theta \leq \theta_3 \\ B_{ge1} - \alpha_2(-\theta + \theta_3)^2 & \theta_3 < \theta \leq \theta_2 \\ B_{gu1} - \alpha_1(-\theta + \theta_1)^2 & \theta_2 < \theta < \theta_1 \\ B_{gu1} & \theta_1 \leq \theta \leq \pi/p \end{cases} \tag{30}$$

$$B_2(\theta) = \begin{cases} B_{gu2} & -\pi/p \leq \theta \leq -\theta_4 \\ B_{gu2} + \alpha_3(\theta + \theta_4)^2 & -\theta_4 < \theta \leq -\theta_5 \\ B_{ge2} - \alpha_4(\theta + \theta_6)^2 & -\theta_5 < \theta \leq -\theta_6 \\ B_{ge2} & -\theta_6 < \theta \leq \theta_6 \\ B_{ge2} - \alpha_4(-\theta + \theta_6)^2 & \theta_6 < \theta \leq \theta_5 \\ B_{gu2} + \alpha_3(-\theta + \theta_4)^2 & \theta_5 < \theta < \theta_4 \\ B_{gu2} & \theta_4 \leq \theta \leq \pi/p \end{cases} \tag{31}$$

where $\alpha_1, \alpha_2, \alpha_3,$ and α_4 are coefficients.

3.2. Armature Reaction

When the DAL-ECR is braking, the rotating magnetic field induces the eddy current in the stator. The induced eddy current density in upper and lower surfaces in the stator slot are as follows:

$$J_1(\theta) = r_5\sigma\omega B_{\delta 1}(\theta) \tag{32}$$

$$J_2(\theta) = r_1\sigma\omega B_{\delta 2}(\theta) \tag{33}$$

where $\sigma, \omega, B_{\delta 1}(\theta),$ and $B_{\delta 2}(\theta)$ are the conductivity of the stator, the angular velocity, and the upper and the lower total air-gap flux density.

The MMF generated by the eddy current will affect the size and distribution of the original air-gap magnetic field generated by the excitation coil. Therefore, the upper and the lower total air-gap flux density are obtained as follows:

$$B_{\delta 1}(\theta) = B_1(\theta) + B_{i1}(\theta) \tag{34}$$

$$B_{\delta 2}(\theta) = B_2(\theta) + B_{i2}(\theta) \tag{35}$$

where $B_1(\theta), B_2(\theta), B_{i1}(\theta),$ and $B_{i2}(\theta)$ are the upper air-gap flux density by the excitation coil, the lower air-gap flux density by the excitation coil, the upper air-gap flux density by the eddy current, and the lower air-gap flux density by the eddy current, respectively.

Figure 6a shows the effective reaction flux lines. The FEM shows that the eddy current is concentrated in a small depth near the air gap under transient condition, as shown in Figure 7. Therefore, as shown in Figure 6b, the MMF generated in the region of the eddy current density in upper and lower surfaces in the stator slot can be given by

$$F_{i1} = \oint_{c_1} Hdl = \int_{\theta I}^{\theta II} \int_{r_5}^{r_5+\Delta_1} J_1(r, \theta) r dr d\theta \tag{36}$$

$$F_{i2} = \oint_{c_2} Hdl = \int_{\theta III}^{\theta IV} \int_{r_1}^{r_1+\Delta_2} J_2(r, \theta) r dr d\theta \tag{37}$$

where c_1 is the integral loop of the magnetic field intensity in the upper part of the stator, c_2 is the integral loop of the magnetic field intensity in the lower part of the stator as shown in Figure 6b, Δ_1 is the skin depth of the upper part of stator in transient state, and Δ_2 is the skin depth of the lower part of stator in transient state.

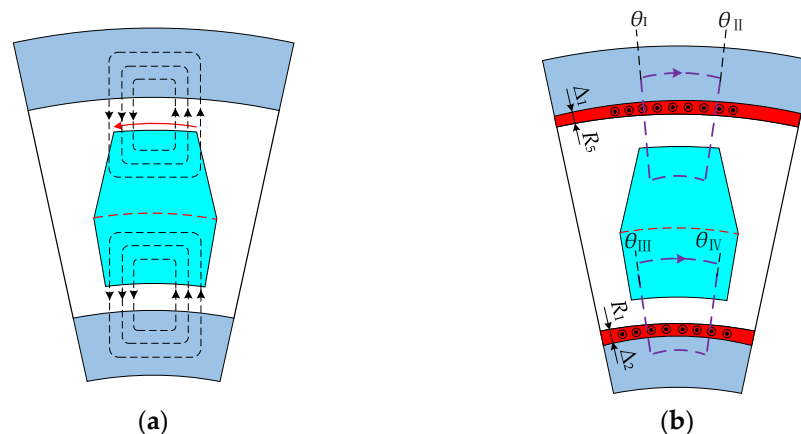


Figure 6. (a) Magnetic flux lines of the armature reaction. (b) Integral closed path of the contour integral in Ampere’s law.

Figure 8 shows that the magnetic field is concentrated in a small skin depth. The skin depth can be given by

$$\Delta = \sqrt{\frac{2}{\omega\mu\sigma}} \tag{38}$$

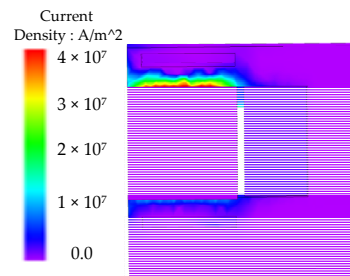


Figure 7. Eddy current density distribution in the stator at 1000 r/min with a current of 80 A.

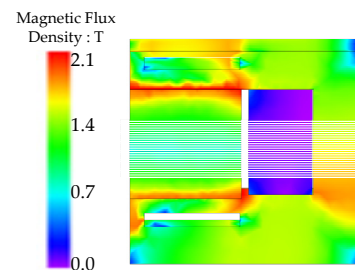


Figure 8. Magnetic flux density distribution in the stator at 1000 r/min with a current of 80 A.

The permeability of the stator and the rotor is much higher than those of the air gap. Therefore, the MMF drops across the stator, and the rotor can be ignored. Hence, Equations (36) and (37) can be transformed into:

$$2\delta B_{i1}(\theta) / \mu_0 = \int_{\theta_I}^{\theta_{II}} \int_{r_{s1}}^{r_{s1}+\Delta_1} \sigma\omega^2 r_{r1}^2 B_{\delta 1}(\theta) drd\theta \tag{39}$$

$$2\delta B_{i2}(\theta) / \mu_0 = \int_{\theta_{III}}^{\theta_{IV}} \int_{r_{s2}-\Delta_1}^{r_{s2}} \sigma\omega^2 r_{r2}^2 B_{\delta 2}(\theta) drd\theta \tag{40}$$

Taking Equations (32) and (33) into Equations (39) and (40), respectively, the following equations can be given:

$$\begin{cases} B_{i1}(\theta) = u_1 \int_{\theta_I}^{\theta_{II}} [B_1(\theta) + B_{i1}(\theta)] d\theta \\ u_1 = \frac{\sigma\omega\mu_0 [(r_{s1}+\Delta_1)^3 - r_{s1}^3]}{6\delta} \end{cases} \tag{41}$$

$$\begin{cases} B_{i2}(\theta) = u_2 \int_{\theta_{III}}^{\theta_{IV}} [B_2(\theta) + B_{i2}(\theta)] d\theta \\ u_2 = \frac{\sigma\omega\mu_0 [r_{s2}^3 - (r_{s2}-\Delta_2)^3]}{6\delta} \end{cases} \tag{42}$$

Taking the derivative of the Equations (41) and (42) with respect to θ , the following equations can be obtained:

$$dB_{i1}(\theta) / d\theta - u_1 B_{i1}(\theta) = u_1 B_1(\theta) \tag{43}$$

$$dB_{i2}(\theta) / d\theta - u_2 B_{i2}(\theta) = u_2 B_2(\theta) \tag{44}$$

When $\pm\pi/P < \theta < \pm\theta_2$ and $\pm\pi/P < \theta < \pm\theta_5$, the air gap value is large, and the reaction magnetic field in these regions can be assumed to be 0 T. Hence, Equations (43) and (44) only applicable to $-\theta_2 < \theta < \theta_2$ and $-\theta_5 < \theta < \theta_5$. Finally, the upper and lower air-gap flux density generated by the eddy current can be given, respectively, by

$$B_{i1} = \begin{cases} B_{i(1-1)} = 0 & -\pi/p < \theta < -\theta_1 \\ B_{i(1-2)} = 0 & -\theta_1 < \theta < -\theta_2 \\ B_{i(1-3)} = k_{1-3}e^{u_1\theta} + \alpha_2\theta^2 + \left(\frac{2\alpha_2+2u_1\alpha_2\theta_3}{u_1}\right)\theta + \frac{2\alpha_2+2u_1\alpha_2\theta_3}{u_1^2} + \alpha_2\theta_3^2 - B_{ge1} & -\theta_2 < \theta < -\theta_3 \\ B_{i(1-4)} = k_{1-4}e^{u_1\theta} - B_{ge1} & -\theta_3 < \theta < \theta_3 \\ B_{i(1-5)} = k_{1-5}e^{u_1\theta} + \alpha_2\theta^2 + \left(\frac{2\alpha_2-2u_1\alpha_2\theta_3}{u_1}\right)\theta + \frac{2\alpha_2-2u_1\alpha_2\theta_3}{u_1^2} + \alpha_2\theta_3^2 - B_{ge1} & \theta_3 < \theta < \theta_2 \\ B_{i(1-6)} = 0 & \theta_2 < \theta < \theta_1 \\ B_{i(1-7)} = 0 & \theta_1 < \theta < \pi/p \end{cases} \quad (45)$$

$$B_{i2} = \begin{cases} 0 & -\pi/p < \theta < -\theta_4 \\ 0 & -\theta_4 < \theta < -\theta_5 \\ B_{i(2-3)} = k_{2-3}e^{u_2\theta} + \alpha_4\theta^2 + \left(\frac{2\alpha_4+2u_2\alpha_4\theta_6}{u_2}\right)\theta + \frac{2\alpha_4+2u_2\alpha_4\theta_6}{u_2^2} + \alpha_4\theta_6^2 - B_{ge2} & -\theta_5 < \theta < -\theta_6 \\ B_{i(2-4)} = k_{2-4}e^{u_2\theta} - B_{ge2} & -\theta_6 < \theta < \theta_6 \\ B_{i(2-5)} = k_{2-5}e^{u_2\theta} + \alpha_4\theta^2 + \left(\frac{2\alpha_4-2u_2\alpha_4\theta_6}{u_2}\right)\theta + \frac{2\alpha_4-2u_2\alpha_4\theta_6}{u_2^2} + \alpha_4\theta_6^2 - B_{ge2} & \theta_6 < \theta < \theta_5 \\ 0 & \theta_5 < \theta < \theta_4 \\ 0 & \theta_4 < \theta < \pi/p \end{cases} \quad (46)$$

where, $k_{1-3}, k_{1-4}, k_{1-5}, k_{2-3}, k_{2-4}$, and k_{2-5} are coefficients.

The boundary conditions for solving Equations (45) and (46) are given, respectively:

$$\begin{cases} B_{i(1-4)}(\theta_{0-1}) = 0 \\ B_{i(1-2)}(-\theta_2) = B_{i(1-3)}(-\theta_2) \\ B_{i(1-3)}(-\theta_3) = B_{i(1-4)}(-\theta_3) \\ B_{i(1-4)}(\theta_3) = B_{i(1-5)}(\theta_3) \end{cases} \quad (47)$$

$$\begin{cases} B_{i(2-4)}(\theta_{0-2}) = 0 \\ B_{i(2-2)}(-\theta_5) = B_{i(2-3)}(-\theta_5) \\ B_{i(2-3)}(-\theta_6) = B_{i(2-4)}(-\theta_6) \\ B_{i(2-4)}(\theta_6) = B_{i(2-5)}(\theta_6) \end{cases} \quad (48)$$

where θ_{0-1} is a special point where the all currents in the upper stator enclosed in the intervals $[-\pi/p, \theta_{0-1}]$ and $[\theta_{0-1}, \pi/p]$ are equal, and θ_{0-2} is a special point where the all currents in the lower stator enclosed in the intervals $[-\pi/p, \theta_{0-2}]$ and $[\theta_{0-2}, \pi/p]$ are equal.

3.3. 3-D Correction

In fact, the distribution of the eddy current in the stator is very complex. To consider this problem, an effective conductivity value [14] is introduced that is given by

$$\sigma = K_n\sigma_c \quad (49)$$

$$K_n = 1 - \frac{2\tanh\varepsilon}{\varepsilon(1 + \tanh\varepsilon\tanh\phi)} \quad (50)$$

$$\varepsilon = \frac{pL_1}{2r_3} \quad (51)$$

$$\phi = \frac{p(L_2 - L_1)}{4r_3} \tag{52}$$

3.4. Transient Permeability Correction

To consider the transient permeability of the stator, the iterative method of transient permeability is introduced, as shown in Figure 9.

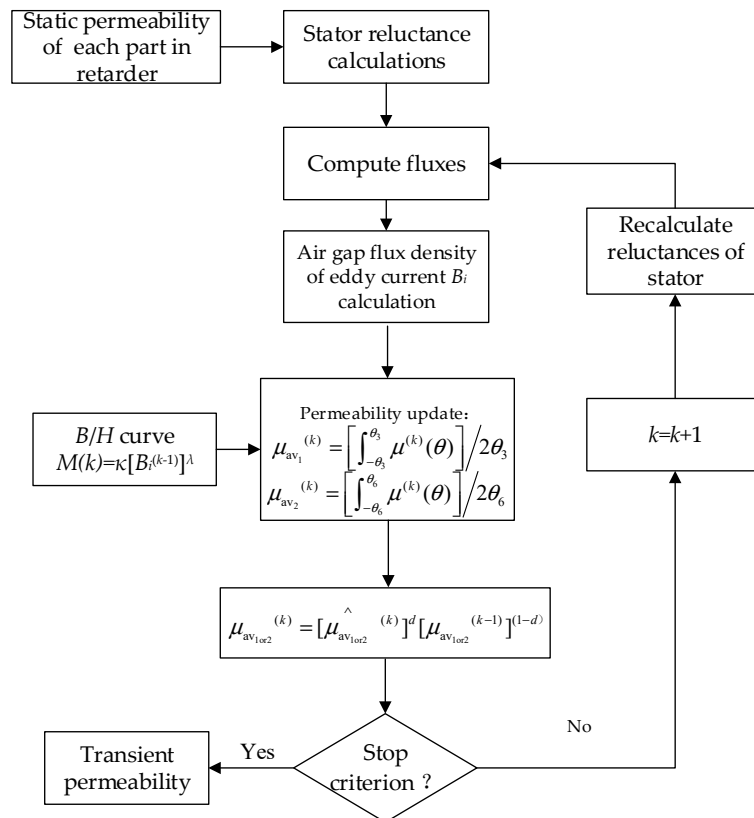


Figure 9. Iterative flowchart of the transient permeability of ferromagnet.

The iterative flowchart is used to determine the transient permeability. It starts by assigning an initial value to $\mu_1, \mu_2, \mu_3, \mu_4, \mu_5,$ and μ_6 to determine the static reluctance network and compute the fluxes. The permeabilities of each part of the retarder are solved by the previous iteration method [1,15].

The working speed of retarders is often greater than 500 r/min, and skin depth of the stator is very small, which means that the magnetic field intensity value is quite high. However, the magnetic force is not provided by the magnetic field by coil, but by the eddy current in the stator. Therefore, the air-gap flux density of the eddy current is equal to the flux density in the stator [27].

Next, based on Equations (45) and (46), the air-gap magnetic flux densities are calculated and used as magnetic flux densities in the depth of the skin.

Then, based on the B/H curve of the utilized steel and eddy current magnetic field of retarder in operation, new permeabilities can be updated by

$$\mu^{(k)} = \kappa [B_i^{(k-1)}]^\lambda \tag{53}$$

where k refers to the iteration time, κ is the proportional index (0.255 herein), λ is the exponential coefficient (−12 herein). Due to magnetic saturation in retarder stator, κ and λ were set to 0.255 and −12, respectively, to accurately fit the magnetic saturation section in

the B/H curve. Since equation is a continuous function, the average permeability in upper and lower surfaces in the stator can be obtained by

$$\mu_{av_1}^{(k)} = \left[\int_{-\theta_3}^{\theta_3} \mu^{(k)}(\theta) \right] / 2\theta_3 \quad (54)$$

$$\mu_{av_2}^{(k)} = \left[\int_{-\theta_6}^{\theta_6} \mu^{(k)}(\theta) \right] / 2\theta_6 \quad (55)$$

The process continues until the following criteria are individually satisfied for the permeabilities of the R_2 and the R_6 :

$$\mu_{av}^{(k)} = [\mu_{av}^{(k-1)}]^d [\mu_{av}^{(k-1)}]^{(1-d)} \quad (56)$$

$$\left[\mu_{av}^{(k)} - \mu_{av}^{(k-1)} \right] / \mu_{av}^{(k-1)} \leq 0.01 \quad (57)$$

where d is a damping constant set to 0.1 herein.

3.5. Eddy Current Braking Torque

The eddy current braking torque can be given by

$$P = \left(L_2 / \sigma \omega^2 \right) \left(\int_0^{2\pi} \int_{r_5}^{r_5+\Delta_1} [J_1(r, \theta)]^2 r dr d\theta + \int_0^{2\pi} \int_{r_1}^{r_1+\Delta_2} [J_2(r, \theta)]^2 r dr d\theta \right) \quad (58)$$

4. FEM Verification

To verify the correctness of the proposed analysis model, the DAL-ECR is simulated by FEM. The main design parameters and material properties of the DAL-ECR are shown in Tables 1 and 2.

Table 1. Geometrical parameters of the DAL-ECR.

Parameters	Value	Parameters	Value
r_0	100 mm	h_3	9 mm
r_1	145 mm	h_4	19 mm
r_2	145.5 mm	L_1	70 mm
r_3	180 mm	L_2	80 mm
r_4	214.5 mm	L_3	64 mm
r_5	215 mm	L_4	30 mm
r_6	240 mm	L_5	50 mm
h_1	8.5 mm	L_6	45 mm
h_2	19 mm	δ	0.5 mm

Table 2. Physical parameters stator and rotor at 25 °C.

Material	ρ (kg/m ³)	σ_c (S/m)	c_s (J/kg·K)	λ (W/m·K)
10CrMo	7870	5×10^6	460	44

Figures 10 and 11 show that the static upper and lower air-gap flux density with a current of 80 A predicted by the proposed method are in good agreement with that calculated by the FEM.

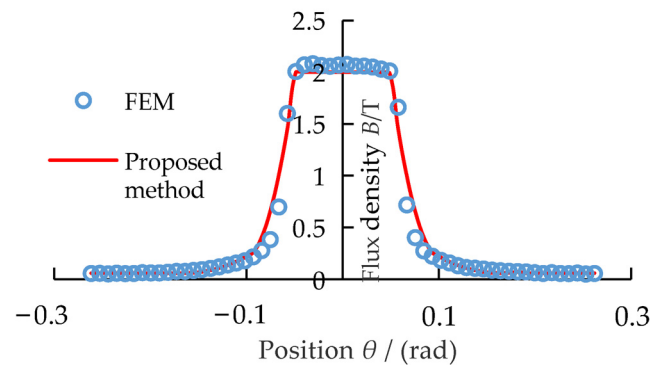


Figure 10. FEM and proposed model predicted the static upper air-gap flux density waveform diagram with a current of 80 A.

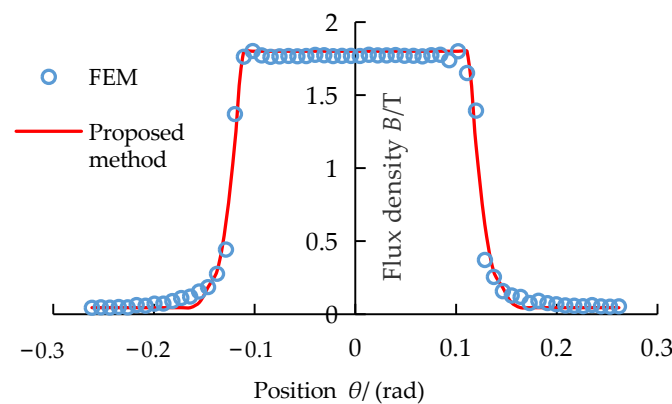


Figure 11. FEM and proposed model predicted the static lower air-gap flux density waveform diagram with a current of 80 A.

As can be seen from Figure 12, when the excitation current of the coil is 80 A and the rotating speed is 500 r/min, the upper air-gap flux density calculated by the proposed method considering transient permeability is closer to the FEM calculating value than that calculated by the proposed method neglecting transient permeability. Especially in the range from 0.04 to 0.07 rad, the upper air-gap flux density calculated by the proposed method considering transient permeability shows its advantages.

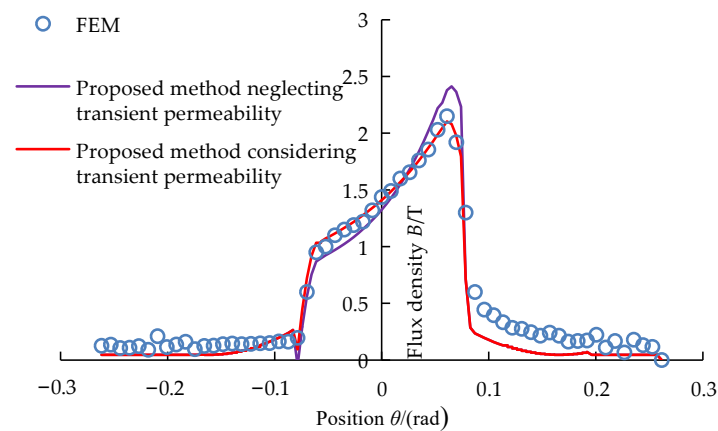


Figure 12. FEM and proposed model predicted the upper air-gap flux density at 500 r/min with a current of 80 A.

Figure 13 shows that when the speed is 500 r/min and the excitation current is 80 A, the lower air-gap flux density calculated by the proposed method is in good agreement with that calculated by the FEM in the entire region. There is no large error like Figure 11 in the local area. However, the lower air-gap flux density calculated by the proposed method neglecting transient permeability is higher than that calculated by the FEM and the proposed method considering transient permeability.

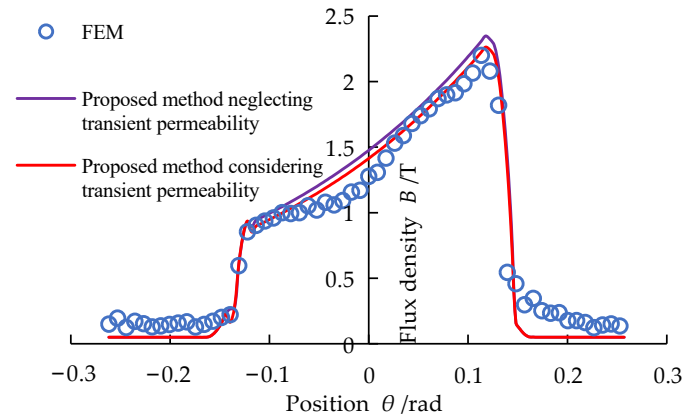


Figure 13. FEM and proposed model predicted air-gap flux density at 500 r/min with a current of 80 A.

As observed from Figure 14, when the speed is 1000 r/min and the excitation current is 80 A, the upper air-gap flux density calculated by the proposed method neglecting transient permeability differs significantly from the FEM value. With the increase of speed, the error of the models increases. However, the error of the mathematical model without considering the transient permeability is larger, especially in the range of from 0.06 to 0.08 rad.

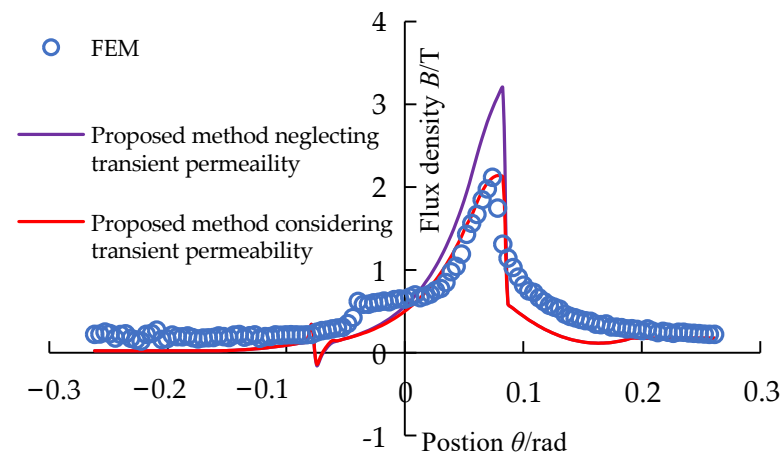


Figure 14. FEM and proposed model predicted the upper air-gap flux density at 1000 r/min with a current of 80 A.

As observed from Figure 15, when the speed is 1000 r/min and the excitation current is 80 A, the lower air-gap flux density calculated by the proposed method neglecting transient permeability is significantly higher than the FEM and the proposed method considering the transient permeability calculated value. However, the lower air-gap flux density by the model considering transient permeability is in good agreement with the FEM value.

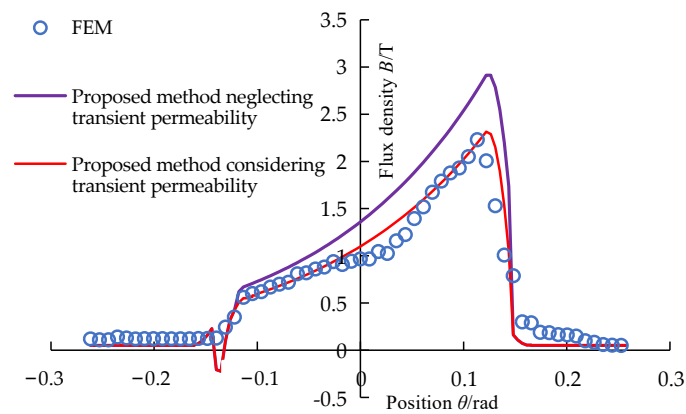


Figure 15. FEM and proposed model predicted the lower air-gap flux density at 1000 r/min with a current of 80 A.

5. Test Bench

5.1. Bench Test System and DAL-ECR Prototype

To test the braking performance of the DAL-ECR and verify the effectiveness of the proposed method, a test bench was set up. The main components of the test bench were the large power driving motor (350 kW), the torque measuring instrument, the temperature sensor, the speed sensor, the water-cooling system, the electric control cabinet, and the data acquisition device, as shown in Figures 16 and 17. Figure 18 shows the DAL-ECR prototype. The number of the excitation coil turns is 105.

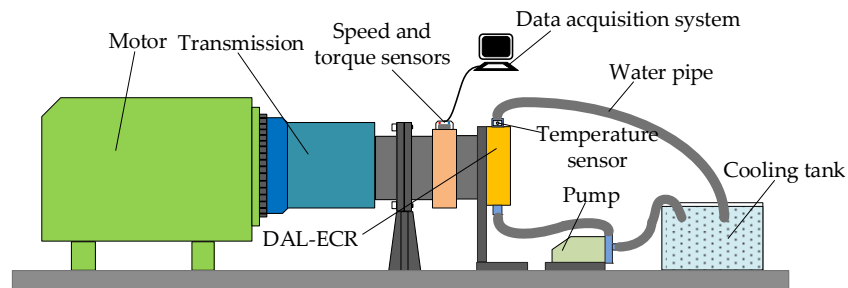


Figure 16. Schematic diagram of the test bench.

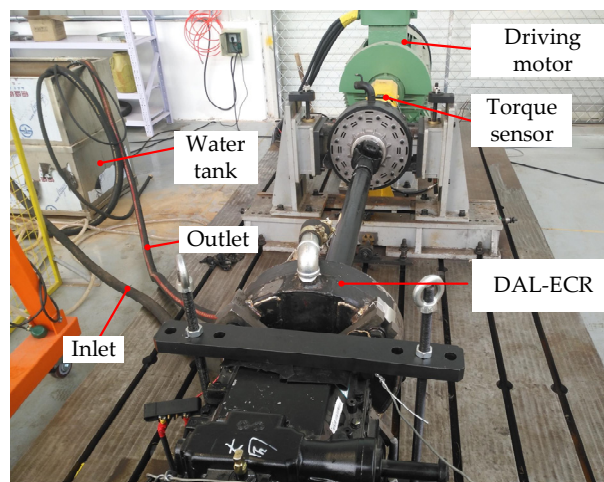


Figure 17. Test bench for the DAL-ECR.



Figure 18. DAL-ECR prototype: (a) stator; (b) rotor.

To control the excitation current size of DAL-ECR, the electronic control unit of the DAL-ECR was developed, as shown in Figure 19. The electronic control unit is able to output different sizes of current through an IGBT control according to different voltage signals.



Figure 19. Electronic control unit of DAL-ECR.

5.2. Torque Characteristics of DAL-ECR

5.2.1. Braking Torque to Eliminate Temperature Effects and Model Validation

During the experiment, the speed of the driving motor was first set to 250 r/min and, after the speed was stabilized, the excitation current was adjusted to 15 A through the DAL-ECR electronic control unit and the stable torque value was recorded. The braking torque was recorded once every 250 r/min increase in speed until the speed reached 2000 r/min. The current of the DAL-ECR was adjusted to 25 A, 50 A, and 80 A in turn, and the above test process was repeated so as to obtain the relationship curve between the braking torque and the speed of each current. The DAL-ECR used water cooling to greatly reduce the influence of heat on the braking torque, but to eliminate the influence of high temperature as much as possible the flow rate of cooling water was set to approximately 200 L/min, and the ECR was completely cooled to the room temperature before the next group of tests.

As shown in Figure 20, the braking torque of the DAL-ECR increases with the increase of the excitation current. The braking torque of different excitation current increases with the increase of speed, and its growth rate decreases continuously, and the lower the excitation current, the more obvious this phenomenon. When the excitation current is 80 A and the speed is 2000 r/min, the braking torque of the DAL-ECR reaches 1620 N·m.

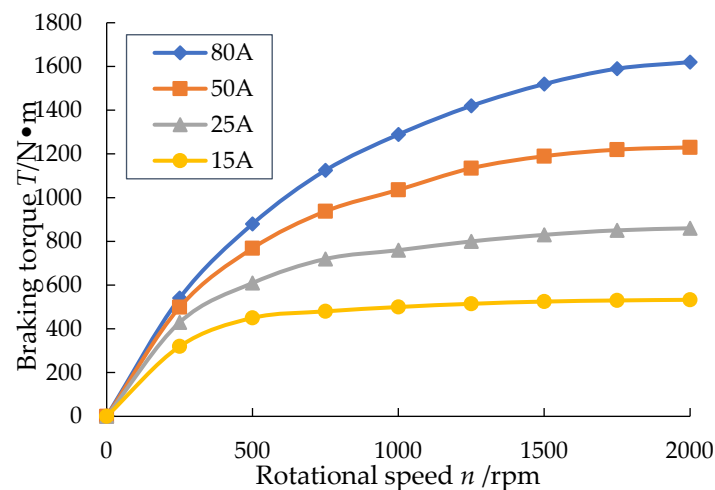


Figure 20. The relationship between braking torque, speed, and excitation current.

As can be seen from Figure 21, when the excitation current is 80 A, the water temperature is in the 20–45 °C, and speed is lower than 500 r/min, the value of the braking torque calculated by the proposed method considering transient permeability, the value calculated by the proposed method neglecting transient permeability, and the value calculated by FEM are in good agreement with the value obtained by the experiment. However, when the speed is higher than 750 r/min, with the increase of rotational speed the error in the proposed method considering transient permeability, the error in the proposed method neglecting transient permeability, and the error in FEM gradually increase, while the error for the proposed method neglecting transient permeability is the largest among the three methods. The maximum calculation error of the proposed method considering transient permeability is 21% and the average error is 13.7%. Compared to the method neglecting transient permeability, the method considering transient permeability has no obvious advantage at low speed. However, with the increase of speed, the skin effect of the electromagnetic field in the retarder components becomes more serious, and the advantages of the method are gradually obvious.

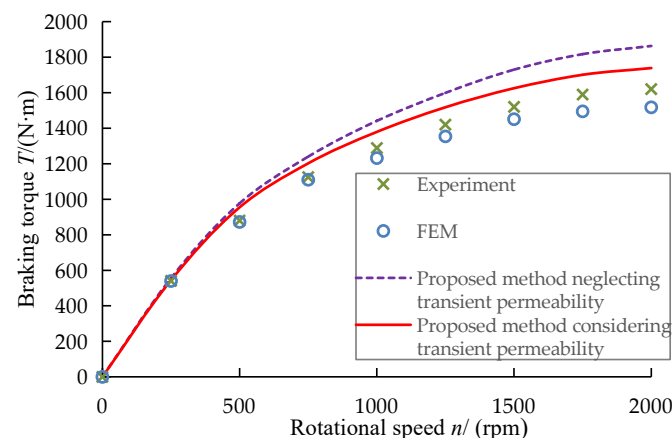


Figure 21. Comparison curve of the proposed method, FEM, and the experimental results of the braking torque for the water temperature in the range of 20–45 °C.

5.2.2. Torque Thermal Decay Characteristics

ECRs mainly work on the long downhill continuous braking condition of heavy vehicles; the speed is generally controlled at 35~40 km/h. Therefore, according to the transmission ratio and wheel radius of the heavy vehicles, the working speed range of ECRs can be obtained in the range of 1500~2000 r/min. Therefore, when the torque thermal decay performance test of DAL-ECR was carried out, the test speed was set to 1500 r/min;

the test was continued for 12 min; and the speed, the braking torque, the temperature, and the braking time were recorded. As shown in Figure 22, the DAL-ECR continued braking for 12 min and the coolant temperature increased by 45 °C, indicating that the liquid cooling heat dissipation kept the DAL-ECR operating at a lower temperature. After continuous braking for 12 min, the braking torque of DAL-ECR decreased from 1520 Nm to 1083 Nm, and the braking torque thermal decreased by 28.75%.

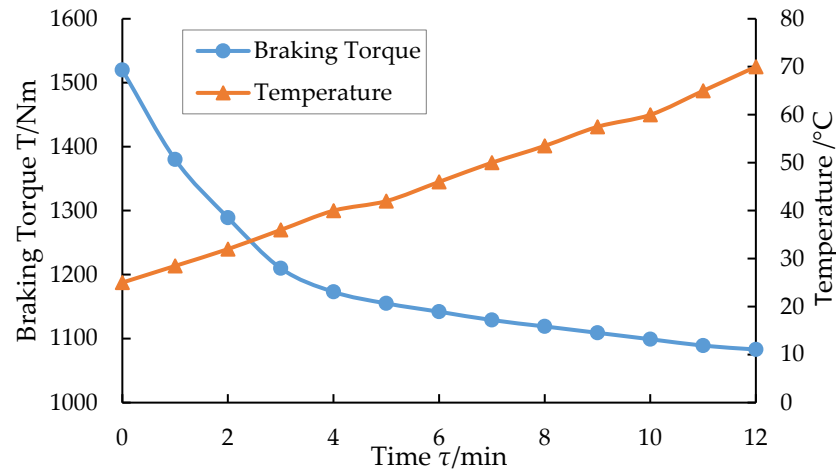


Figure 22. Variation of braking torque and temperature with time.

6. Discussion

As observed from Figures 12–15, compared with the upper air-gap flux density calculated by the proposed method, the lower air-gap flux density calculated by the proposed method is in better agreement with the FEM. This is due to the high magnetic saturation in the stator part corresponding to the upper air gap. With the speed increasing, the calculation accuracy of the proposed method becomes worse. This is because the eddy current magnetic field increases with the increase of the speed, resulting in the inconsistent distribution of circumferential permeability on the stator material. However, the proposed model only considers the change of radial permeability with speed and does not consider the change of circumferential permeability distribution with speed.

As can be seen from Figure 21, the braking torque model considering the transient permeability has obvious advantages over the model without considering the transient permeability at high speed. When the retarder is running at high speed, the electromagnetic field in the stator will have a strong skin effect, resulting in a sharp decrease in the permeability of the stator. In this case, even if the speed increases again, the braking torque will not increase significantly. When the speed increases to a certain value, the braking torque will tend to be stable. Therefore, the decrease of permeability caused by the skin effect is an important factor limiting the eddy current braking performance. On the other hand, due to ignoring the influence of heat, the proposed model cannot predict the torque during continuous braking of DAL-ECR.

ECRs mainly works in the long downhill continuous braking condition of heavy vehicles, the speed is generally controlled at 35–40 km/h, and the braking torque is not less than 1500 Nm. Therefore, according to the transmission ratio and wheel radius of the heavy vehicles, the working speed range of the ECR can be obtained in the range of 1500–2000 r/min. When the working speed of the DAL-ECR is within the above speed range and the excitation current is 80 A, the braking torque range is 1520–1620 Nm, as shown in Figure 20. Taking into account the actual capacity of the vehicle battery, the operating current of the ECR generally does not exceed 100 A, so the maximum test current set does not exceed 80 A during the bench test. In addition, the DAL-ECR uses an independent water tank to dissipate heat, and the coolant temperature is controlled at 20–70 °C. The cooling system of the liquid-cooled ECR can also be connected with

the cooling system of the engine, so to achieve common heat dissipation of the two, this cooling method will make the coolant temperature control at 80–98 °C. Compared with the independent cooling method, this cooling method will make the brake torque of the retarder smaller.

7. Conclusions

This paper proposed a fast prediction model of the braking performance of the DAL-ECR considering the flux leakage, end effect, and transient permeability, and the calculation accuracy of the model was verified by the FEM and the bench test. The model has no obvious advantage at low speed. However, with the increase of speed, the advantages of the model are gradually obvious.

The proposed method is suitable for the prediction of air-gap flux density with over saturation of excitation and is only suitable for the prediction of eddy current braking of liquid-cooled ECR. Hence, the method has some limitations.

Author Contributions: Methodology, W.G. and B.Y.; software, W.G. and B.Y.; writing—original draft preparation, W.G. and B.Y.; writing—review and editing, W.G. and B.Y.; validation, D.L. and W.G.; data curation, W.G. and D.L. All authors have read and agreed to the published version of the manuscript.

Funding: This research was funded by Key Research Projects of Higher Education Institutions in Henan Province and grant number [22B460001], and the Doctoral Start-up Funding of Anyang Institute of Technology and grant number [40076212].

Data Availability Statement: Not applicable.

Acknowledgments: The authors gratefully acknowledge the support they received from the Key Research Projects of Higher Education Institutions in Henan Province and the Doctoral Start-up Funding of Anyang Institute of Technology (22B460001, 40076212).

Conflicts of Interest: The authors declare no conflict of interests. The funders had no role in the design of the study; in the collection, analyses, or interpretation of data; in the writing of the manuscript; or in the decision to publish the results.

References

1. Anwar, S. A parametric model of an eddy current electric machine for automotive braking application. *IEEE Trans. Control Syst. Technol.* **2004**, *12*, 422–427. [[CrossRef](#)]
2. Hofmann, M.; Werle, T.; Pfeiffer, R.; Binder, A. 2D and 3D numerical field computation of eddy-current brakes for traction. *IEEE Trans. Magn.* **2000**, *36*, 1758–1763. [[CrossRef](#)]
3. Fujita, M.; Tokumasu, T.; Yamada, T.; Hirose, T.; Tanaka, Y.; Kumagai, N.; Uchida, S. 3-dimensional electromagnetic analysis and design of an eddy-current rail brake system. *IEEE Trans. Magn.* **1998**, *34*, 3548–3551. [[CrossRef](#)]
4. Sharif, S.; Faiz, J.; Sharif, K. Performance analysis of a cylindrical eddy current brake. *IET Electr. Power Appl.* **2012**, *6*, 661–668. [[CrossRef](#)]
5. Tian, J.; Li, D.; Ning, K.; Ye, L. Research on heat dissipation optimization of a novel liquid-cooling eddy current brake. *IEEE Trans. Energy Convers.* **2021**, *36*, 131–138. [[CrossRef](#)]
6. Jiao, B.; Li, D.; Du, X.; Zhang, K. Performance analysis and experimentation of a liquid-cooled eddy current retarder with a dual salient poles design. *IEEE Trans. Energy Convers.* **2014**, *29*, 84–90. [[CrossRef](#)]
7. Ye, L.; Liu, Y.; Li, D. Optimization design and test of dual air-gaps and liquid-cooled eddy current retarder. *Int. J. Appl. Electron.* **2019**, *61*, 157–170. [[CrossRef](#)]
8. Gay, S.; Ehsani, M. Parametric analysis of eddy-current brake performance by 3-D finiteelement analysis. *IEEE Trans. Magn.* **2006**, *53*, 8110205.
9. Takahashi, N.; Natsumeda, M.; Muramatsu, K.; Yamada, C.; Ogawa, M.; Kobayashi, S.; Kuwahara, T. Optimization of permanent magnet type of retarder using 3-D finite element method and direct search method. *IEEE Trans. Magn.* **1998**, *34*, 2996–2999. [[CrossRef](#)]
10. Ereamus, A.; Kamper, M. Computationally efficient analysis of double PM-rotor radial flux eddy current couplers. *IEEE Trans. Ind. Appl.* **2017**, *53*, 3519–3527.
11. Cho, S.; Liu, H.; Ahh, H.; Lee, J.; Lee, H. Eddy Current Brake with a Two-Layer Structure: Calculation and Characterization of Braking Performance. *IEEE Trans. Magn.* **2017**, *42*, 319–328. [[CrossRef](#)]

12. Shin, H.; Choi, J.; Cho, H.; Jang, S. Analytical torque calculations and experimental testing of permanent magnet axial eddy current brake. *IEEE Trans. Magn.* **2013**, *49*, 4152–4155. [[CrossRef](#)]
13. Lubin, T.; Rezzoug, A. Steady-state and transient performance of axial-field eddy-current coupling. *IEEE Trans. Ind. Electr.* **2015**, *62*, 2287–2296. [[CrossRef](#)]
14. Gulec, M.; Yolacan, E.; Aydin, E. Design, analysis and real time dynamic torque control of single-rotor-single-stator flux eddy current brake. *IET Electr. Power Appl.* **2016**, *10*, 869–876. [[CrossRef](#)]
15. Jin, Y.; Kou, B.; Li, L.; Li, C.; Pan, D.; Song, K. Analytical model for a permanent magnet eddy-current brake with transverse edge effect. *IEEE Access* **2019**, *5*, 61170–61179. [[CrossRef](#)]
16. Lubin, T.; Rezzoug, A. Improved 3-D analytical model for axial-flux eddy-current couplings with curvature effects. *IEEE Trans. Magn.* **2017**, *53*, 8002409. [[CrossRef](#)]
17. Jin, Y.; Li, L.; Kou, B.; Pan, D. Thermal analysis of a hybrid excitation linear eddy current brake. *IEEE Trans. Ind. Electr.* **2019**, *66*, 2987–2997. [[CrossRef](#)]
18. Ye, L.; Chen, Z.; Ma, Z.; Qiu, H.; Chai, S. Design and test validation of a novel permanent magnet eddy current brake. *Int. J. Appl. Electrom.* **2022**, *70*, 323–344. [[CrossRef](#)]
19. Mohammadi, M.; Mirsalim, M.; Vaez-Zadeh, S. Analytical modeling and analysis of axial-flux interior permanent-magnet couplers. *IEEE Trans. Ind. Electr.* **2014**, *61*, 5940–5947. [[CrossRef](#)]
20. Wang, J.; Zhu, J. A simple method for performance prediction of permanent magnet eddy current couplings using a new magnetic equivalent circuit model. *IEEE Trans. Ind. Electr.* **2018**, *65*, 2487–2495. [[CrossRef](#)]
21. Mohammadi, S.; Mirsalim, M.; Vaez-Zadeh, S. Nonlinear modeling of eddy-current couplers. *IEEE Trans. Energy Convers.* **2014**, *29*, 224–231. [[CrossRef](#)]
22. Mohammadi, S.; Mirsalim, M. Double-sided permanent-magnet radial-flux eddy-current couplers: Three-dimensional analytical modelling, static and transient study, and sensitivity analysis. *IET Electr. Power Appl.* **2013**, *7*, 665–679. [[CrossRef](#)]
23. Gulec, M.; Aydin, M.; Nerg, J.; Lindh, P.; Pyrhönen, J. Magneto-thermal analysis of an axial-flux permanent-magnet-assisted eddy-current brake at high-temperature working conditions. *IEEE Trans. Ind. Electr.* **2021**, *68*, 5112–5121. [[CrossRef](#)]
24. Kou, B.; Chen, W.; Jin, Y. A novel cage-secondary permanent magnet linear eddy current brake with wide speed range and its analytical model. *IEEE Trans. Ind. Electr.* **2022**, *69*, 7130–7139. [[CrossRef](#)]
25. Kou, B.; Jin, Y.; Zhang, H.; Zhang, L.; Zhang, H. Nonlinear analytical modeling of hybrid excitation double sided linear eddy current brake. *IEEE Trans. Magn.* **2015**, *51*, 8003404. [[CrossRef](#)]
26. Guo, W.; Li, D.; Ye, L. A model of magnetic field and braking torque in liquid-cooled permanent-magnet retarder accounting for the skin effect on permeability. *IEEE Trans. Veh. Technol.* **2019**, *68*, 10618–10626. [[CrossRef](#)]
27. Davies, E.J. An experimental and theoretical study of eddy-current couplings and brakes. *IEEE Trans. Power Appar. Syst.* **1963**, *82*, 401–419. [[CrossRef](#)]

Disclaimer/Publisher’s Note: The statements, opinions and data contained in all publications are solely those of the individual author(s) and contributor(s) and not of MDPI and/or the editor(s). MDPI and/or the editor(s) disclaim responsibility for any injury to people or property resulting from any ideas, methods, instructions or products referred to in the content.